Silicon substrate significantly alters dipole-dipole resolution in coherent microscope

ZICHENG LIU AND KRISHNA AGARWAL* (iD)

Department of Physics and Technology, UiT The Arctic University of Norway, NO-9037 Tromsø, Norway
*krishna.agarwal@uit.no

Abstract: Considering a coherent microscopy setup, influences of the substrate below the sample in the imaging performances are studied, with a focus on high refractive index substrate such as silicon. Analytical expression of 3D full-wave vectorial point spread function, i.e. the dyadic Green's function is derived for the optical setup together with the substrate. Numerical analysis are performed in order to understand and compare magnification, depth of field, and resolution when using silicon substrate versus the conventional glass substrate or usually modelled condition of no substrate. Novel insights are generated about the scope of resolution improvement due to near field effect of the silicon substrate. Importantly, we show that the expected resolution varies greatly with the position of the sources and the substrate interface relative to the focal plane. Both better and worse resolution as compared to glass substrate may be expected with small changes in their positions. Therefore, our studies show that deriving a single indicative number of expected resolution is neither possible nor judicious for the case of silicon substrate.

1. Introduction

Fluorescence microscopy and nanoscopy are perturbative, photo-chemically toxic, and limited in photon-budget [1–4]. Therefore, label-free imaging is desired and advancements in resolution and image quality are being prioritized. While classical qualitative label-free imaging techniques such as bright-field, differential interference contrast, and phase contrast still remain popular, new array of quantitative label-free techniques are being developed at a rapid pace. Examples include quantitative phase microscopy [5–12], diffraction tomography and holography [9,12–19], phase gradient [20–22], ptychography or phase retrieval [18,23,24], etc.

Most of these approaches use computational image reconstruction algorithms custom designed for the setup. The algorithms in turn require some or other form of mathematical mapping function which maps the points in the sample to the scalar field distribution in the image region, often referred to as the point spread function (PSF). Often scalar PSFs are used [7,25,26]. However, 3D full-wave vector point spread function, referred to as dyadic Green's function (DGF), have also been considered [27–29]. As compared to the assumption of scalar point sources in the case of PSF, the DGF maps point dipoles of known orientations to the vectorial electric field in image region. Due to the assumption of dipole sources, DGF holds additional potential in comparison to scalar PSF in considering the local polarization effects in the sample region.

DGFs have been derived and investigated for homogeneous medium in the sample region [28,29]. DGF of special configurations such as solid immersion lens have also been investigated [30] and channelized for improving resolution [31] through identification of roles and relative contributions of different polarizations induced in the sample region [32]. These formulations neglect one inevitable aspect of microscopy for biological imaging, that is the presence of an interface due to the resting surface of sample. For example, biological sample is places in a petri dish, as shown in Fig. 1(a) or on a glass slide. The importance of modeling the interface has been recognized before, and incoherent point spread functions of optical microscopes have been derived [33]. When using high numerical aperture (NA) liquid (water or oil) immersion objective

lens, the refractive index contrast between the glass substrate and the immersion liquid is small, and therefore the effect on image is negligibly small as verified here in this manuscript. However, recently photonics based substrates and structures have been used to enhance the near field effects and achieve better resolution in fluorescence nanoscopy [8,34–38]. Here, we consider the case where a silicon substrate shown in Fig. 1(b), instead of glass substrate is used for placing the sample as a first step towards understanding the role of high refractive index substrate on the near-field effects and consequently on the image in a microscope.
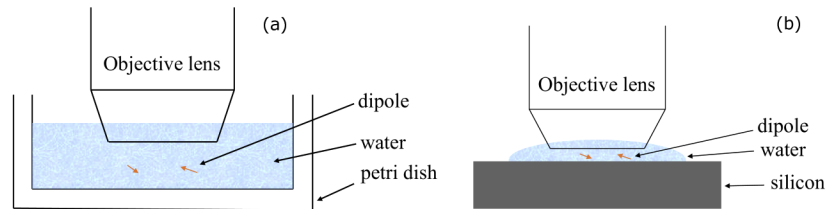

Fig. 1. Sketch of sample region of a microscope with a water immersion objective lens when samples are (a) in petri dish and (b) on the silicon substrate, respectively.

In order to correctly account for the near-field effects of the silicon substrate on the image, it is important to use DGF rather than scalar PSF. It is imperative to include the substrate in the formulation of DGF as an interface that splits the sample region into two half spaces, one where the dipoles can be present in the immersion medium and the other that corresponds to the substrate. We do note that there have been works related to layered medium in optical systems [39] for optical memory and lithography [40] and focusing of lights into stratified medium [41–43]. However, DGF for a microscopy system involving the conventional microscope-objective and tube lens pair is currently not analysed to the best of our knowledge.

Here, the DGF of the concerned microscopy system is solved by analyzing the reflection and refraction behaviors of each plane-wave component and integrating all rays reaching the image region. Based on the closed-form solution of DGF, the lateral and longitudinal resolutions are studied with various settings. In addition to the conventionally investigated resolution assuming lateral dipoles [30], we also considered defining and computing resolution for z-polarized dipoles. This aspect of resolution for z-polarized dipoles is generally considered unamenable to resolution analysis due to their image being annulus shaped rather than spot-like [29]. Our results present new exciting insights into the expectations of resolution when using silicon as the substrate, which turn out to be quite different from glass substrate and are heavily dependent upon the location of the substrate and the dipole sources with respect to the focal plane. We also find that such a substrate can support better resolution than glass substrate in selected conditions, and significantly poorer resolution in other conditions.

2. Setup and notations

Figure 2 presents the schematic diagram and the important notations of the concerned microscopy system. Taking the optical axis as the z axis, two local coordinate systems are built whose origins are located at the focal points of the objective region and the image region, respectively. These regions are respectively created by the objective lens (focused on the sample) and the tube lens (focused on the camera). The notation of quantities in the objective region employs the subscript "obj", while quantities in the image region, where camera sensors (scientific CMOS, CCD or emCCD) are positioned, are subscripted by "cam". Here, the general derivation is being made for the region close to the image plane and the center of camera pixel is used to represent the pixel assuming a pixel to be point-like detector. However, generalization to a large pixel or

optical detector size (such as photodetector or multiphoton diode) can be made by integrating the computed intensity over the area of the detection element.

In the objective region, O_{obj} denotes the focal point, n_{obj} the refractive index of the medium in which sample is kept, k_{obj} the wavenumber, f_{obj} the focal length. $\mathbf{r}'_{\text{obj}}$ denotes the position of a dipole with Cartesian coordinates $[x'_{\text{obj}}, y'_{\text{obj}}, z'_{\text{obj}}]$. $\mathbf{r}^o_{\text{obj}}$ denotes an example observation point in the objective lens region. Here, $\mathbf{r}'_{\text{obj}}$ is defined to facilitate the derivation of the DGF and is not used in the final formulation of DGF. The notations in the image region are similarly defined. The substrate is modeled as the lower half space and characterized by the position of the substrate interface $z_{\text{obj}} = z^b_{\text{obj}}$ (i.e., parallel with the x,y plane) and the refractive index n_{sub}. The angular semiaperture of the objective lens is $\theta^{\max}_{\text{obj}}$. Both the objective lens and the tube lens are represented by Gaussian reference spheres (GRS) [29]. Remark that the vector quantities are noted in bold and notations with double bars above denote tensors with dimension 3×3.
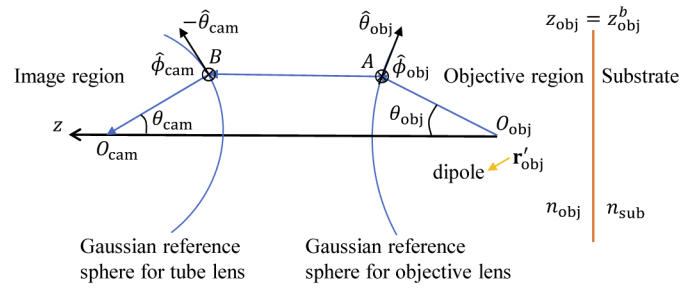

Fig. 2. Optical sketch of aplanatic microscope with a substrate.

3. Solution to dyadic Green's function

As sketched in Fig. 2, a unit dipole polarized along an arbitrary direction $\hat{a}$ locates in the objective region. After reflections by the substrate interface, the emitted waves propagate through the objective lens and the tube lens, and finally recorded at pixel locations on camera array. We denote the field solution as $\mathbf{G}(\mathbf{r}^o_{\text{obj}}, \hat{a})$. The dyadic Green's function (DGF) is defined by $\overline{\overline{G}}\left(\mathbf{r}^o_{\text{obj}}\right) = \left[\mathbf{G}\left(\mathbf{r}^o_{\text{obj}}, \hat{x}\right), \mathbf{G}\left(\mathbf{r}^o_{\text{obj}}, \hat{y}\right), \mathbf{G}\left(\mathbf{r}^o_{\text{obj}}, \hat{z}\right)\right]$, which is a 3×3 tensor. The solution to the DGF of the half space is a superposition of TE (s-polarized) and TM (p-polarized) parts [44],

$$\overline{\overline{G}}\left(\mathbf{r}^o_{\text{obj}}\right) = \iint_{-\infty}^{+\infty} dk_x dk_y \frac{1}{k^z_{\text{obj}}} \left(\overline{\overline{G}}^{\text{TE}} + \overline{\overline{G}}^{\text{TM}}\right) e^{i\mathbf{k}_{\text{obj}}\mathbf{r}^o_{\text{obj}}} \tag{1}$$

in which

$$\overline{\overline{G}}^{\text{TE}} = \frac{1}{8i\pi^2} \hat{\phi}_{\text{obj}}\left(\mathbf{k}_{\text{obj}}\right) \mathbf{K}^{\text{TE}}, \overline{\overline{G}}^{\text{TM}} = \frac{1}{8i\pi^2} \hat{\theta}_{\text{obj}}\left(\mathbf{k}_{\text{obj}}\right) \mathbf{K}^{\text{TM}} \tag{2}$$

See Supplement 1 for the expression of $\mathbf{K}^{\text{TE}}$ and $\mathbf{K}^{\text{TE}}$. $\mathbf{k}_{\text{obj}} = k_x \hat{x} + k_y \hat{y} + k^z_{\text{obj}} \hat{z}$ denotes the wave vector of the integrated plane-wave components and $k^z_{\text{obj}} = \sqrt{k^2_{\text{obj}} - k^2_x - k^2_y}$. $\hat{\phi}_{\text{obj}}\left(\mathbf{k}_{\text{obj}}\right)$ and $\hat{\theta}_{\text{obj}}\left(\mathbf{k}_{\text{obj}}\right)$ are defined as the unit vector of the azimuthal and elevation axis for $\mathbf{k}_{\text{obj}}$.

Since we consider a far-field imaging microscope, i.e., the focal length $f_{\text{obj}} \gg \lambda_{\text{obj}}$, only the far (propagating) fields need to be considered in the integration of 1, i.e., the integral region is restricted by $k^2_x + k^2_y \leq k^2_{\text{obj}}$. With the method of stationary phase [29], the solution of fields (before the refraction by the objective lens) at any point on the objective lens GRS surface **A**, as

sketched in Fig. 2, is solved as

$$\overline{\overline{G}}_\infty(\mathbf{A}) = -\frac{e^{ik_{\mathrm{obj}}f_{\mathrm{obj}}}}{4\pi f_{\mathrm{obj}}} \left[\hat{\phi}_{\mathrm{obj}} \ (A) \ \mathbf{K}^{\mathrm{TE}} + \hat{\theta}_{\mathrm{obj}} \ (\mathbf{A})\mathbf{K}^{\mathrm{TM}} \right] \tag{3}$$

Following the sine condition and the intensity law [29], after the refraction by the objective lens and the tube lens, the field at the tube lens GRS surface **B** is with expression

$$\overline{\overline{G}}_\infty(\mathbf{B}) = c_1 \sqrt{\frac{\cos \theta_{\mathrm{obj}}^A}{\cos \theta_{\mathrm{cam}}^B}} \left[\hat{\phi}_{\mathrm{cam}}(\mathbf{B})\mathbf{K}^{\mathrm{TE}} - \hat{\theta}_{\mathrm{cam}}(\mathbf{B})\mathbf{K}^{\mathrm{TM}} \right] \tag{4}$$

where c_1 is a constant, and θ_{obj}^A, θ_{cam}^B are the elevation angle of **A** and **B**, respectively. The superposition of all rays from the surface of the tube lens yields the solution of DGF, i.e.,

$$\overline{\overline{G}}\left(\mathbf{r}_{\mathrm{cam}}^o\right) = c_2 \int_0^{\theta_{\mathrm{obj}}^{\mathrm{max}}} \int_0^{2\pi} \overline{\overline{G}}_\infty e^{i\mathbf{k}_{\mathrm{cam}}\mathbf{r}_{\mathrm{cam}}^o} \frac{\sin 2\theta_{\mathrm{obj}}}{\cos \theta_{\mathrm{cam}}} d\phi_{\mathrm{obj}} d\theta_{\mathrm{obj}} \tag{5}$$

where only plane-wave components with the elevation angle smaller than the angular semiaperture $\theta_{\mathrm{obj}}^{\mathrm{max}}$ are integrated. See Supplement 1 for the expression of each element of $\overline{\overline{G}}$.

4. Investigations on resolution

Effects of the half space are studied by setting the refractive index of the lower half space as $n_{\mathrm{sub}} = 4.3$ (silicon) or 1.52 (glass), while the objective region is with $n_{\mathrm{obj}} = 1.33$ (water) and the camera sensors are in the air, i.e., $n_{\mathrm{cam}} = 1$. The wavelength in vacuum is chosen as $\lambda = 500$ nm and focal length $f_{\mathrm{obj}} = 1$ cm, $f_{\mathrm{cam}} = 10$ cm. The lateral magnification is $M^{\mathrm{lat}} = 13.3$ (See Supplement 1 for the derived expression of M^{lat}). Where not stated explicitly, the NA of the system is assumed to be 1.

4.1. Investigation of lateral resolution

Here, we investigate the lateral resolution of the setup shown in Fig. 2. Sections 4.1.1 and 4.1.2 present the quantification of resolution for laterally oriented and longitudinally oriented (i.e. z-polarized) dipoles. The comparison of lateral resolution for the glass and silicon substrates is presented in section 4.1.3. Interesting insights with regard to resolution variability in the case of silicon substrate are also provided.

4.1.1. Lateral resolution for x-polarized or y-polarized dipoles

The (induced) charge of dipoles can have a high variance in the analysis of imaging performance [45]. To get rid of effects from values of charge, normalization is performed. Considering electric fields at points $\mathbf{r}_{\mathrm{cam}}^{(i)}, i = 1, \ldots, N$, the normalized electric fields equal $\mathbf{E}(\mathbf{r}_{\mathrm{cam}}^{(i)})/E^{\mathrm{max}}$, $E^{\mathrm{max}} = \max\{|\mathbf{E}(\mathbf{r}_{\mathrm{cam}}^{(i)})| : i = 1, \ldots, N\}$ and the related quantities are denoted by putting a bar above, i.e., $\bar{\mathbf{E}} = \mathbf{E}/E^{\mathrm{max}}$. The normalized field due to two dipoles is computed as $\bar{\mathbf{E}}(\mathbf{r}_{\mathrm{cam}}^{(i)}, \mathbf{r}_{\mathrm{obj}}^{1,\prime}) + \bar{\mathbf{E}}(\mathbf{r}_{\mathrm{cam}}^{(i)}, \mathbf{r}_{\mathrm{obj}}^{2,\prime})$, where $\bar{\mathbf{E}}(\mathbf{r}_{\mathrm{cam}}^{(i)}, \mathbf{r}_{\mathrm{obj}}^{s,\prime})$ denotes the normalized field due to the s-th dipole. Thus, the intensity of combined fields may have maximum not equal to 1. The normalization discussed here applies throughout the article. The silicon substrate is used in the example settings in Fig. 3.

Imaging resolution is investigated from the intensity values in the image region when two dipoles are located near the focal point O_{obj}. Based on the image of two adjacent dipoles, as sketched by Fig. 3(a), the saddle-to-peak ratio $I_{\mathrm{min}}/I_{\mathrm{max}}$ is computed, where I_{max} is the maximum intensity of the combined field and I_{min} the minimum between two peaks. According to the modified Rayleigh limit, the resolution is defined as the minimum distance between two dipoles when the ratio is ≤ 0.735.
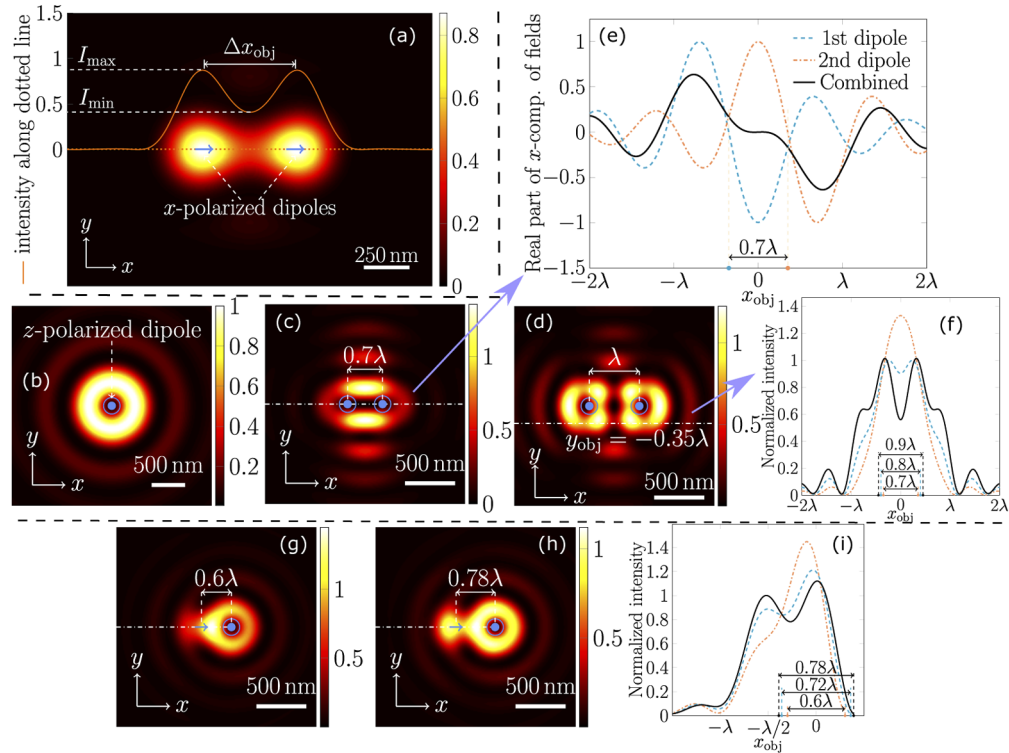
Fig. 3. Definition of lateral resolution for different combinations of dipole orientations.
When the silicon substrate is positioned 500 nm below the focal plane and the dipoles on the focal plane with Cartesian coordinates $[\pm\Delta x_{\mathrm{obj}}/2, 0, 0]$, (a) shows the image of two resolvable x-polarized dipoles. Resolution is defined as the minimum of Δx_{obj} when $I_{\min}/I_{\max} \leq 0.735$. (b) Image of a z-polarized dipole is an annulus. (c) Image of two unresolvable dipoles, small intensities between the dipoles due to destructive interference in (e). (d) Image of resolvable z-polarized dipoles. (f) Sampled intensities along the dashed lines in (d) have decreased saddle-to-peak ratio with increasing distance between dipoles. (g,h) Images of the x, z-polarized dipoles indicate that resolution can be quantified from the sampled intensities along the dash-dotted lines. The fact that the saddle-to-peak ratio decreases with the increasing distance between the two dipoles in (i) leads to the applicability of modified Rayleigh limit for quantifying resolution. For the reference of the reader, the conventional value of resolution in the incoherent case, given by Abbe is $\lambda/(2\mathrm{NA}) = 250$ nm.

4.1.2. Lateral resolution for z-polarized dipoles

The aforementioned criterion is based on the assumption that the image of a dipole is spot-like. This is true for *x*-polarized and *y*-polarized dipoles. However, as shown by Fig. 3(b), the image of a *z*-polarized dipole is an annulus, which makes the above method for quantifying resolution inapplicable. We consider potential solution for defining resolution in the situation where at least one of the dipoles is z-polarized. Two cases are considered, both the dipoles directed towards $\hat{z}$ and one of them directed to $\hat{x}$. The *y*-polarized dipoles are not considered due to similar behavior with *x*-polarized dipoles and straightforward generalizability.

Case 1: Two z-polarized dipoles Two dipoles are placed at $(-\Delta x_{\mathrm{obj}}/2, 0, 0)$ and $(\Delta x_{\mathrm{obj}}/2, 0, 0)$, respectively. In Fig. 3(c), we consider the situation when two *z*-polarized dipoles are separated by distance $\Delta x_{\mathrm{obj}} = 0.7\lambda$ (i.e., 350 nm). Even though the image of each dipole independently looks like an annulus, the image of two dipoles in vicinity is not a superimposition of two annuli. Small intensities in the region between the dipoles are due to destructive interferences. Along the *x* axis, we determined that the intensity value is mainly contributed from the real part of the *x*-component of electric fields, denoted by E_x, which is plotted in Fig. 3(e). One observes that destructive interference occurs due to the opposite signs of $\mathfrak{R}(E_x)$ in the region between the dipoles.

As the distance Δx_{obj} is increased, the signature of two dipoles becomes quite evident even though the image still does not look like a simple super-imposition of two annuli. Figure 3(d) shows the image when $\Delta x_{\mathrm{obj}} = \lambda$. Based on the observations in Fig. 3(f), we propose that the resolvability of two *z*-polarized dipoles separated along x-axis can be inferred using the intensity profile along the line defined by $z_{\mathrm{cam}} = 0$ and $y_{\mathrm{cam}} = \pm y_{\mathrm{cam}}^{\mathrm{peak}}$, as shown by the dash-dotted line in Fig. 3(d). Here, $y_{\mathrm{cam}}^{\mathrm{peak}}$ is the distance of the peak values of intensities along *y* axis to the center of the annulus and can be numerically determined. Figure 3(f) shows the variation of the sampled intensities when the two dipoles are moved further from each other along this line for the example configuration used in this paper. The decreased saddle-to-peak ratio with the increasing distance between the emitters reveals that the modified Rayleigh limit computed over the line defined by $z_{\mathrm{cam}} = 0$ and $y_{\mathrm{cam}} = \pm y_{\mathrm{cam}}^{\mathrm{peak}}$ can now be used for quantifying the resolution for the case of two *z*-polarized dipoles.

Case 2: One x- and one z-polarized dipoles: Images of the situation when a *x*-polarized dipole and a *z*-polarized are presented in the sample region are shown in Figs. 3(g,h). As seen, the only indicator of the presence of two dipoles is the asymmetry in the intensity profile in Fig. 3(g) whereas the presence of two dipoles is evident from the intensity profile in Fig. 3(h). Considering that the image of a z-polarized dipole is an annulus and not a spot, the observations for quantifying the resolution are taken along a line segment that starts at the center of the annulus and extends beyond the peak corresponding to the other dipole, such as shown using the dash-dotted lines in Figs. 3(g,h). This is contrary to considering a line segment that passes through both of the dipoles in the case of only x-polarized or y-polarized dipoles as well as considering a line that passes through the peak of annuli parallel to the locations of dipole in the case of two z-polarized dipoles. As shown in Fig. 3(i), as the distance Δx_{obj} increases, the initially merged peak splits into two peaks and the saddle-to-peak ratio decreases. The modified Rayleigh limit can therefore be applied. However, it is important to remark that the location of peaks of sampled intensities does not correspond to the accurate position of dipoles.

4.1.3. Comparison of resolution for silicon and glass substrates

Since *x*-polarized and *y*-polarized dipoles behave similarly (see Supplement 1), we focus on the 4 representative cases for studying lateral resolution. These are with polarizations $\{\mathbf{p}_1 = \hat{x}, \mathbf{p}_2 = \hat{x}\}$, $\{\mathbf{p}_1 = \hat{x}, \mathbf{p}_2 = \hat{y}\}$, $\{\mathbf{p}_1 = \hat{z}, \mathbf{p}_2 = \hat{z}\}$, and $\{\mathbf{p}_1 = \hat{x}, \mathbf{p}_2 = \hat{z}\}$, where $\mathbf{p}_i$ is the direction of the *i*-th

dipole, $i = 1, 2$. The second case is due to the fact that it may have significantly higher resolution than the first case.

Setting the positions of dipoles are $(-\Delta x_{\text{obj}}/2, 0, z'_{\text{obj}})$ and $(\Delta x_{\text{obj}}/2, 0, z'_{\text{obj}})$, the modified Rayleigh limit is obtained by increasing Δx_{obj} with the step 0.02λ and taking the minimal Δx_{obj} when the saddle-to-peak ratio is ≤ 0.735. We assume that two dipoles have the distance to the focal plane less than or equal to λ and the substrate interface is below the focal plane up to 2λ, i.e. $z^b_{\text{obj}} \in (0, -2\lambda]$. The results without the presence of half space are also included for comparisons.

The estimated resolution in Fig. 4 is quantified in λ. The region bounded by white dashed lines and filled with black represents the non-physical condition when the dipoles are below the substrate interface and therefore not applicable for study. The estimated resolutions with the glass substrate are presented in Figs. 4(e-h). Due the small refractive index difference with water, the variation of resolution follows the similar phenomena with the situation when no presence of the substrate (the associated results in Fig. 4(j)). The common observations consistent between the no-substrate and glass-substrate are presented here. In particular, we report the observations related to the resolution in the four cases when the z-location of the dipoles is changed. The resolution tends to be better when the two x-polarized dipoles and the x, z-polarized dipoles get closer to the focal plane. For the two z-polarized dipoles, the estimated resolutions range from 0.86λ to 0.9λ. The resolution for the x, y-polarized dipoles is a constant, except the cases which provide strong evidences for the dependency on the distance between the dipoles and the substrate interface. Moreover, for all considered settings of z'_{obj} and z^b_{obj}, the x, y-polarized two dipoles are imaged with the best resolution.

As seen from Figs. 4(a-d), the above-mentioned traits also appear with the silicon substrate. Examples are indicated by the dashed lines in Figs. 4(a,c,d). However, the high contrast of silicon (relative to water) leads to more complex trends. For instance, the resolution of the two x-polarized dipoles only has small variations when $\left| z'_{\text{obj}} \right| \leq 0.4\lambda$, but is very sensitive to the position of substrate when the dipoles are moved further (see Visualization 1). Irrespective of the dipole polarization, the microscope with the silicon substrate shows a larger range of resolution than with the glass substrate. Interestingly, it can achieve higher resolutions for the best cases. Examples are given in Figs. 4(m,n), where the two x-polarized dipoles are not well separated in the images without the substrate but are clearly distinguishable using the silicon substrate.

The estimations in Fig. 4 also reveal that samples on the focal plane may have lower-resolution images than those off the plane depending upon the position of the interface. Figures 4(k,l) show that the non-resolvable x-polarized dipoles on the focal plane becomes resolvable when the dipoles are on the plane 0.6λ lower.

4.2. Investigations related to longitudinal resolution

Here, we investigate longitudinal aspects imaging, including depth of field (section 4.2.1), longitudinal magnification (section 4.2.2), and lastly longitudinal resolution (section 4.2.3). Attention to comparison of silicon and glass substrates is given. Both the longitudinal magnification and the resolution provide surprising results for the silicon substrate, which are discussed in detail.

4.2.1. Depth of field (DOF)

Depth of field is investigated by moving the position of a dipole along the optical axis. The substrate interface is assumed at the plane $z^b_{\text{obj}} = -2$ μm. As shown in Figs. 3(a,b), the image of a dipole at the focal point is a focused spot or an annulus with small side lobes. When the dipoles have the distance of 1.5λ to the focal plane, as presented in Figs. 5(a,c), the images become out of focus with high side lobes. We note also that the peak intensity is decreased as light spreads wider. We sample the intensities along the y axis since higher slide lobes are observed along the y axis than x axis for the x-polarized dipole. For the silicon substrate, Figs. 5(b,d) are obtained by
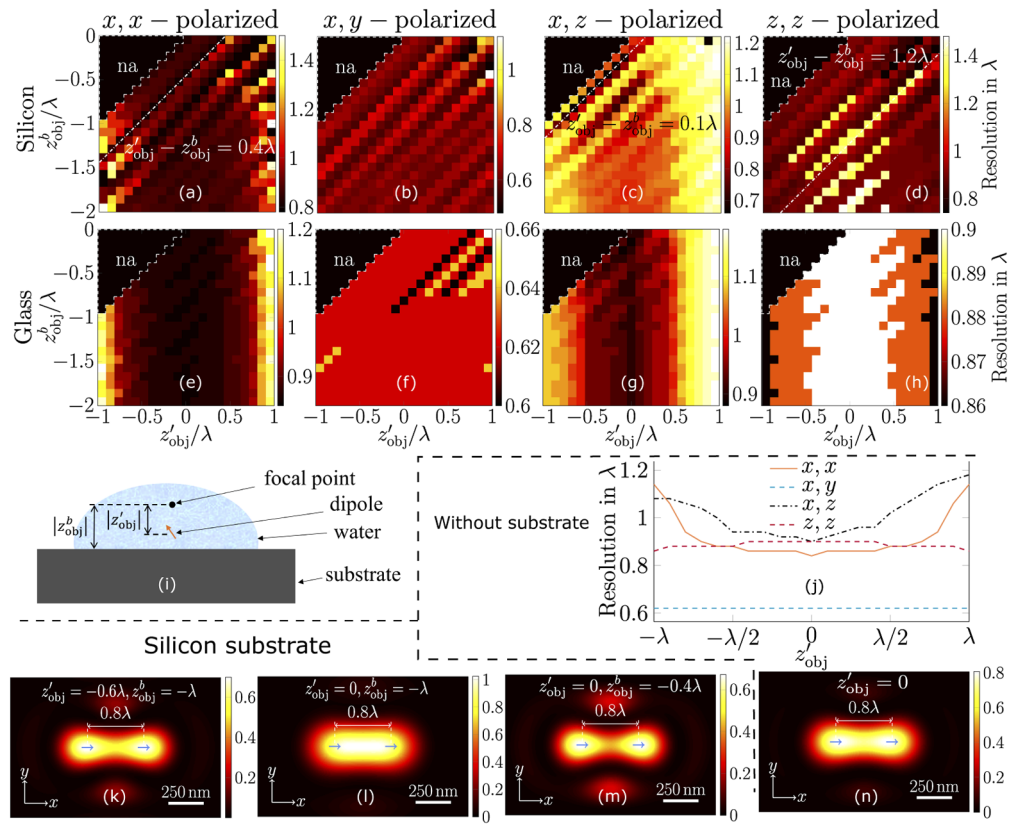
Fig. 4. Study of lateral resolution by varying the position of dipoles and the substrate. Undefined cases when dipoles are below the substrate are labeled with "na". Figures (a-d) are obtained with the silicon substrate and (e-h) are with the glass substrate. Four sets of dipole polarization are considered for each substrate. Cases on the dashed lines are examples of the observation that the lateral resolution is much impacted by the distance between the dipole and the substrate surface. (i) explains the involved notations. (j) gives results without substrate. (k-m) are examples showing effects from the vertical position of the dipoles and the position of the silicon substrate. (m,n) show that higher resolution is reached with the presence of silicon substrate in the sample region.

varying the position of *x* and *z* dipoles, respectively. Similarly, for the glass substrate, Figs. 5(e,f) present the results obtained by shifting the *x* and *z* dipoles, respectively. Despite the polarization and the substrate material, the peak values, which are the intensities along the dashed lines, tend to decrease when the dipole moves further from the focal plane. Since small peak values indicate defocused images, FWHM (full width at half maximum) of the line graphs is used to qualitatively measure the depth of field.
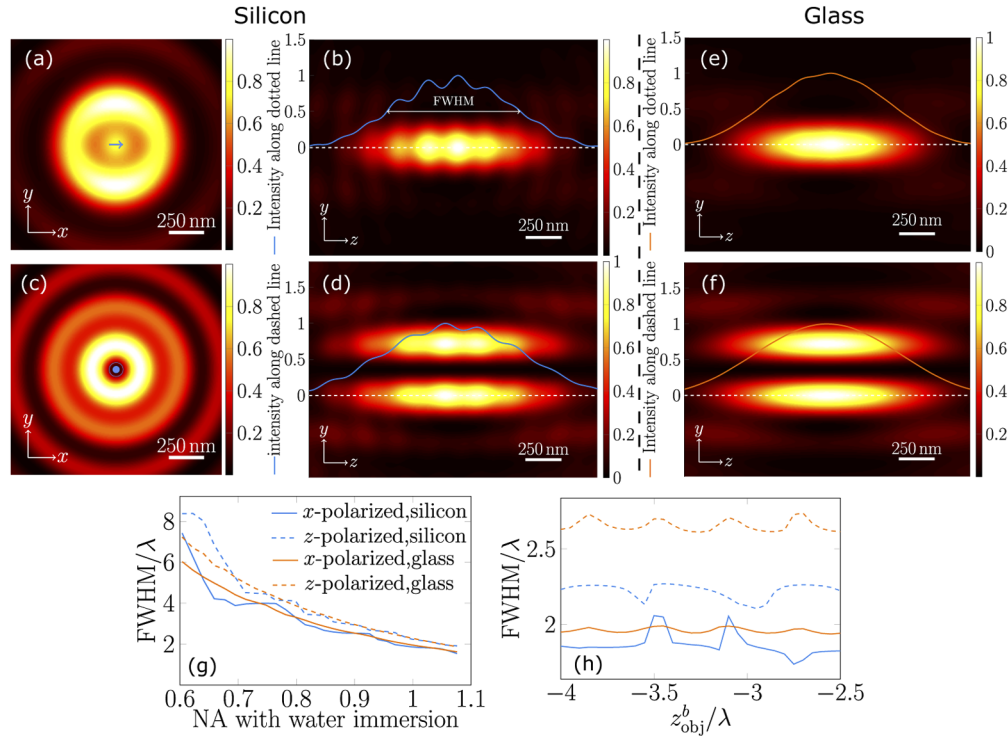

Fig. 5. Comparison of depth of field for silicon and glass substrates. With the silicon substrate 2 μm below the focal plane, (a) gives an example of defocused image of the *x*-polarized dipole which is with coordinates $[0, 0, 1.5\lambda]$. (b) observations along *y* axis with varied vertical positions of the dipole, the peak intensity tends to decreases when the dipole moves further from focal plane. (c,d) present results for the *z*-polarized dipole and (e,f) shows when the medium of substrate is glass. (g,h) show the variation of FWHM of the lines of peak values with increasing numerical aperture (NA) and varied position of substrate.

The above results are with NA= 1. Keeping the immersion medium as water, the effects of numerical aperture is studied by varying the angular semiaperture. As seen from Fig. 5(g), the DOF reduces with the increasing NA. We also note that even though the DOF is usually reported as a single number, the sensitivity to the polarization of the dipole is not often reported such as done here. The variation of DOF when using glass or silicon substrate is not significant in Fig. 5(g). The *x*-polarized dipole generally have smaller DOF than the *z*-polarized dipole. Figure 5(h) shows the sensitivity of the DOF to the location of the distances of the interface from the focus. We note a certain oscillatory behaviour of the value of DOF, which is more prominent in the case of silicon as compared to the glass substrate.

4.2.2. Longitudinal magnification

Supplement 1 provides the derivation of lateral and longitudinal magnification. The general derivation of longitudinal resolution employs paraxial approximation and neglects reflections from the substrate, which may be not valid. Based on the derived formula of Eq. (S13), we have the longitudinal magnification $M^{\mathrm{lon}} = 133$ for the concerned situation, i.e., water immersion and $f_{\mathrm{cam}}/f_{\mathrm{obj}} = 10$. However, this estimation is strongly deviant from the numerical estimations in Fig. 6, which are obtained by putting a x-polarized dipole at $[0, 0, z'_{\mathrm{obj}}]$ and identifying the location of maximum intensity. Since NA= 1, the paraxial approximation is invalid. Without the substrate, the estimations show that M^{lon} is a constant and equals 159.6 when $\left| z'_{\mathrm{obj}} \right| \leq 0.9\lambda$. The presence of the substrate has great impact on the longitudinal magnification. With the glass substrate, strongly fluctuated estimations are obtained when the dipole is close to the focal plane and the magnification ranges from 63.84 to 255.36. With the silicon substrate, the variation extent is even larger. Since the location of the optical detector is fixed and generally matched to the focal plane of the tube lens, this observation may not have significant practical implications in the current microscopy system designs. However, this observation can be very interesting and even exploitable if measurements are taken by axially shifting the optical detector.
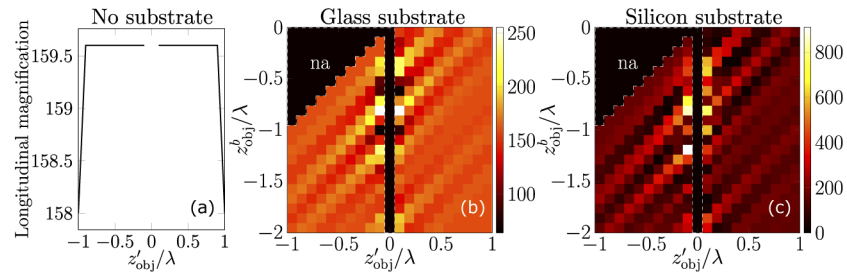

Fig. 6. Comparison of longitudinal magnification for different substrates. (a)When NA= 1 and $\left| z'_{\mathrm{obj}} \right| \leq 0.9\lambda$, the longitudinal magnification is estimated as 159.6. (b) With the glass substrate, the estimated magnification has strong fluctuations with the position of the substrate when $\left| z'_{\mathrm{obj}} \right| \leq 0.2\lambda$. Undefined cases (i.e. the dipoles below the substrate or $z'_{\mathrm{obj}} = 0$) are marked "na". (c) Estimations with silicon substrate.

4.2.3. Longitudinal resolution for silicon and glass substrates

The longitudinal resolution is studied by putting two dipoles at the optical axis but separated by distance Δz_{obj}, which is increased from 0 by the step 0.02λ. When $z^b_{\mathrm{obj}} < -\Delta z_{\mathrm{obj}}$, the two dipoles are assumed with z coordinates $-\Delta z_{\mathrm{obj}}/2$ and $\Delta z_{\mathrm{obj}}/2$, respectively. Otherwise, the z coordinates equal z^b_{obj} and $z^b_{\mathrm{obj}} + \Delta z_{\mathrm{obj}}$ to ensure two dipoles are above the substrate. Figures 7(a-d) show the variation of saddle-to-peak ratio with the increasing distance between dipoles and the varied position of the substrate. The ratio is set as 1 when the two dipoles cannot be clearly distinguished. This may happen in two cases, first if the image of the two dipoles appears as a single spot and second if the electric fields due to the two dipoles interfere such that the side lobes are quite prominent. As seen, the position of the glass substrate has little impact to imaging (witnessed as hardly any variation along the vertical axis in Figs. 7(a,b)) but greater influence of the position of the interface is observed when the silicon substrate is used.

For the results of x, y-polarized dipoles shown in Figs. 7(a,c), the ratio monotonically decreases as the distance between dipoles is larger with the glass substrate. However, for the x, x-polarized dipoles, the saddle-to-peak ratio shows oscillatory behaviors which can make the two dipoles unresolvable even when the distance is larger than the modified Rayleigh limit, which is determined
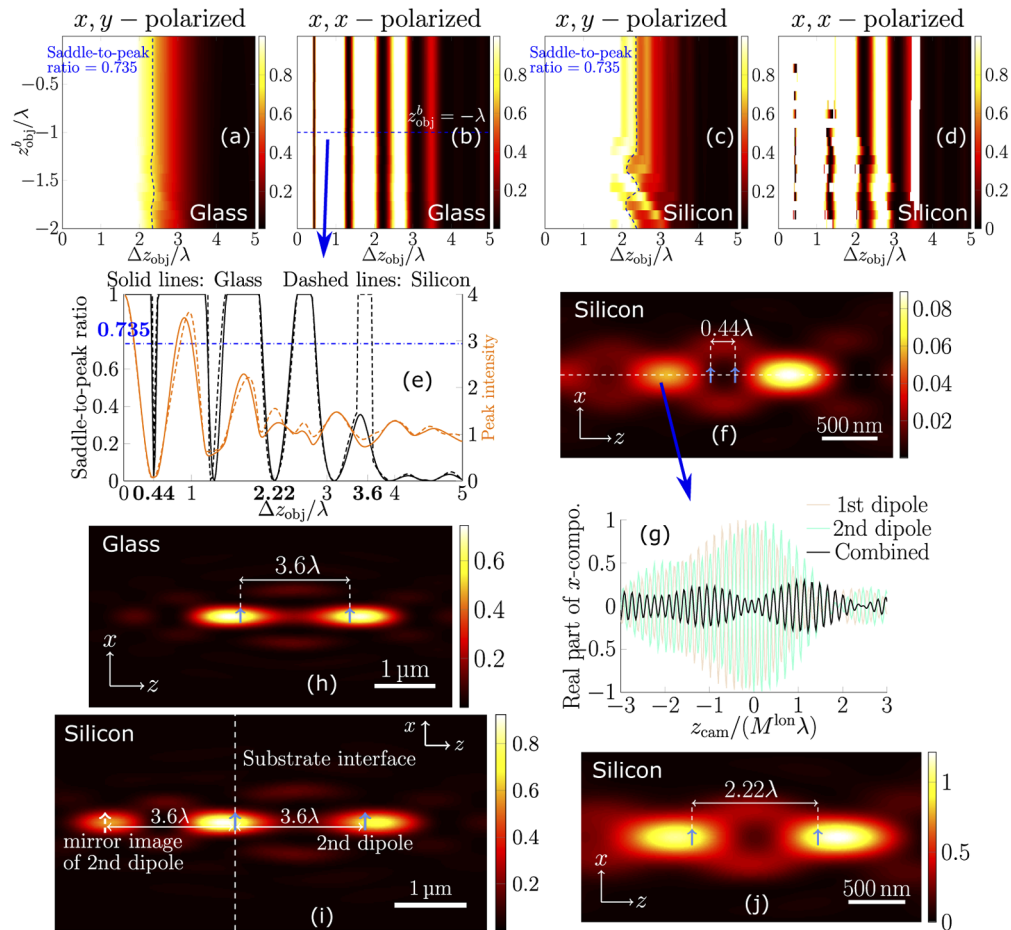
Fig. 7. Investigation of longitudinal resolution. (a,c) Variation of saddle-to-peak ratio with increasing distance between the x, y-polarized dipoles and different positions of the substrate interface. The dashed lines indicate the modified Rayleigh limit. (b,d) show the variation of saddle-to-peak ratio for the two x-polarized dipoles. Sampling the ratios for the situation when $z^b_{obj} = -\lambda$, (e) reveals that the oscillatory behaviors of saddle-to-peak ratio is accompanied with the fluctuations of the peak intensity. As shown in (f,g), the 1st minimum in (e) is due to destructive inference and the spot locations mismatch the positions of the dipoles. (j) shows the image corresponding with the 3rd minimum, where the peak intensity is large and the spot locations indicate the position of the dipoles. (i) reveals that when $\Delta z_{obj} = 3.6\lambda$, the mirror-image of the 2nd dipole is distinguished and three spots are observed with the silicon substrate. (h) Due to the small refractive index contrast for glass substrate, the mirror-image of the 2nd dipole contributes small intensities.

by the threshold of 0.735. The oscillatory behaviors have been reported before [46,47] and explained by observing the intensity at the focal point of the image region. Detailed explanations are given in Supplement 1.

Figure 7(e) includes plots of two different quantities. Plots in black indicate the saddle to peak ratios from Figs. 7(b,d) at the line section shown in Fig. 7(b), which corresponds to $z_{obj}^b = -\lambda$. Plots in orange indicate the peak intensity seen in the image of the two dipoles in the $x - z$ plane as a function of $\Delta z_{obj}/\lambda$ when the interface is at $z_{obj}^b = -\lambda$. In Fig. 7(e), we see that the oscillatory behaviors of saddle-to-peak ratio are accompanied with the fluctuations of the peak intensity, which is related with the image contrast. Figure 7(f) shows the image of the two x-polarized dipoles, the locations of which correspond to the first minimum when the dipoles are separated by distance 0.44λ. Although two spots are seen, the peak intensity is very small and the positions of spots mismatch the positions of dipoles. This phenomenon is explained from observations of the sampled electric fields along the dashed line. Figure 7(g) describes the real part of the x component of electric fields. The fields behave as modulated sinusoids with a high (spatial) frequency. The explanation of such phenomenon is given in Supplement 1. The electric fields due to the two dipoles interfere destructively, as seen in Fig. 7(g). Consequently, a minimum amplitude is observed between the dipoles and leads to the resolvability. However, it should be noted that the positions of the peak values are shifted. In contrast, when the separation is increased as 2.22λ, as shown by Fig. 7(j), the peak intensity is much larger and we can distinguish the locations of the dipoles.

Another interesting case in Fig. 7(e) is the situation of $\Delta z_{obj} = 3.6\lambda$. In this case, the value of saddle-to-peak ratio with the glass substrate indicates two resolvable x-polarized dipoles, the image of which shown in Fig. 7(h). Using the silicon substrate, the ratio is estimated as 1 since there are three spot-like patterns and we may mistakenly conclude that three sources are placed in the objective. This phenomenon is due to the presence of the distinguishable mirror image of the 2nd dipole, as illustrated in Fig. 7(i) (also Visualization 2). The reflection by the substrate is electromagnetically equivalent to the emission by a mirror-image dipole [48]. The positions of the mirror-image dipole and the corresponding true dipole are symmetric about the substrate interface. The 1st dipole in Fig. 7(i) also has a mirror image, which is just merged with the image of the true dipole as a single spot. With the glass substrate, due to its small refractive index contrast with the immersion medium, the reflection by the substrate is weak. As a result, the mirror images have small intensities and are likely to be treated as weak side lobes.

A final observation is derived when observing Figs. 7(a-d) together with the DOF values seen in Fig. 5(h), we see that the regions where the saddle-to-peak ratios are less than 0.735 consistently are also the regions outside the DOF. In other words, resolution of two axially separated dipoles should not be expected if they are within the DOF and is not useful outside the DOF due to small intensities in the image field.

5. Conclusion

The dyadic Green's function (DGF) is solved as multiple Sommerfeld integrals. Our formulation includes the effect of reflections from the substrate over which the sample rests as well as realistically high numerical aperture for high NA water immersion systems. This allows us to emulate the 3D full-field effects and thereby more accurately study the resolution and the other effects, especially as a consequence of using high refractive index substrate such as silicon.

The lateral resolution is found dependent on the polarization of dipoles and also the position of the substrate interface in the case of silicon substrate. It is also demonstrated that such variation can be neglected when using glass substarte because of small refractive index contrast with water medium. It is also noted that simply using a high refractive index substrate can alter the range of resolution significantly. Our results clearly indicate the potential of having signficantly superior resolution: $\sim 0.5\lambda$ for a pair of x- and y-polarized dipoles when using silicon substrate,

as compared to ∼ 0.6λ for glass substrate (corresponding to a significant 50 nm improvement for λ = 500 nm). Yet, for the same dipole orientations, depending upon the distance between them and the with respect to the interface, the resolution may be as poor as ∼ 1.1λ as compared to the poorest resolution for glass surface ∼ 0.66λ. Therefore, caution is preferred while making conclusions on resolution when using high refractive index substrates and structures. On the contrary, the effect of high refractive index substrate on DOF is not quite significant.

For a pair of axially separated *x*-polarized dipoles, the mirror images of the dipoles created due to the high refractive index contrast between the substrate and the medium can be significantly strong and lead to misconclusions on the number of dipoles or their resolvability. Further, the resolution of such dipoles is possible beyond the DOF, where their resolution may be not be useful anyway.

We expect that this analysis and the full-field derivation of DGF will open new avenues for exploring high refractive index materials as substrates for use in coherent microscopy, and at the same time set reasonable expectations about the prospects of using such materials.

Funding

Disclosures

The authors declare no conflicts of interest.

See Supplement 1 for supporting content.

References

1. V. Marx, "Is super-resolution microscopy right for you?" Nat. Methods **10**(12), 1157–1163 (2013).
2. P. C. Montgomery and A. Leong-Hoi, "Emerging optical nanoscopy techniques," Nanotechnol., Sci. Appl. **8**, 31 (2015).
3. J. C. Stockert and A. Blázquez-Castro, *Fluorescence Microscopy in Life Sciences* (Bentham Science Publishers, 2017).
4. A.-L. Robson, P. C. Dastoor, J. Flynn, W. Palmer, A. Martin, D. W. Smith, A. Woldu, and S. Hua, "Advantages and limitations of current imaging techniques for characterizing liposome morphology," Front. Pharmacol. **9**, 80 (2018).
5. G. Popescu, *Quantitative Phase Imaging of Cells and Tissues* (McGraw Hill Professional, 2011).
6. Z. Wang, L. Millet, M. Mir, H. Ding, S. Unarunotai, J. Rogers, M. U. Gillette, and G. Popescu, "Spatial light interference microscopy (SLIM)," Opt. Express **19**(2), 1016–1026 (2011).
7. T. Kim, R. Zhou, L. L. Goddard, and G. Popescu, "Solving inverse scattering problems in biological samples by quantitative phase imaging," Laser Photonics Rev. **10**(1), 13–39 (2016).
8. A. Ahmad, V. Dubey, A. Butola, J.-C. Tinguely, B. S. Ahluwalia, and D. S. Mehta, "Sub-nanometer height sensitivity by phase shifting interference microscopy under environmental fluctuations," Opt. Express **28**(7), 9340–9358 (2020).
9. Y. Park, C. Depeursinge, and G. Popescu, "Quantitative phase imaging in biomedicine," Nat. Photonics **12**(10), 578–589 (2018).
10. A. Anand, V. Chhaniwal, and B. Javidi, "Tutorial: common path self-referencing digital holographic microscopy," APL Photonics **3**(7), 071101 (2018).
11. V. R. Singh, Y. A. Yang, H. Yu, R. D. Kamm, Z. Yaqoob, and P. T. So, "Studying nucleic envelope and plasma membrane mechanics of eukaryotic cells using confocal reflectance interferometric microscopy," Nat. Commun. **10**(1), 3652 (2019).
12. S. Shin, K. Lee, Z. Yaqoob, P. T. So, and Y. Park, "Reference-free polarization-sensitive quantitative phase imaging using single-point optical phase conjugation," Opt. Express **26**(21), 26858–26865 (2018).
13. Y. Cotte, F. Toy, P. Jourdain, N. Pavillon, D. Boss, P. Magistretti, P. Marquet, and C. Depeursinge, "Marker-free phase nanoscopy," Nat. Photonics **7**(2), 113–117 (2013).
14. F. Charrière, A. Marian, F. Montfort, J. Kuehn, T. Colomb, E. Cuche, P. Marquet, and C. Depeursinge, "Cell refractive index tomography by digital holographic microscopy," Opt. Lett. **31**(2), 178–180 (2006).
15. T. Kim, R. Zhou, M. Mir, S. D. Babacan, P. S. Carney, L. L. Goddard, and G. Popescu, "White-light diffraction tomography of unlabelled live cells," Nat. Photonics **8**(3), 256–263 (2014).
16. V. Lauer, "New approach to optical diffraction tomography yielding a vector equation of diffraction tomography and a novel tomographic microscope," J. Microsc. **205**(2), 165–176 (2002).

17. S. Chowdhury, M. Chen, R. Eckert, D. Ren, F. Wu, N. Repina, and L. Waller, "High-resolution 3D refractive index microscopy of multiple-scattering samples from intensity images," Optica **6**(9), 1211–1219 (2019).
18. A. Matlock and L. Tian, "High-throughput, volumetric quantitative phase imaging with multiplexed intensity diffraction tomography," Biomed. Opt. Express **10**(12), 6432 (2019).
19. Y. Kim, J. Jeong, J. Jang, M. W. Kim, and Y. Park, "Polarization holographic microscopy for extracting spatio-temporally resolved jones matrix," Opt. Express **20**(9), 9948–9955 (2012).
20. T. H. Nguyen, M. E. Kandel, M. Rubessa, M. B. Wheeler, and G. Popescu, "Gradient light interference microscopy for 3D imaging of unlabeled specimens," Nat. Commun. **8**(1), 210 (2017).
21. H. Kwon, E. Arbabi, S. M. Kamali, M. Faraji-Dana, and A. Faraon, "Single-shot quantitative phase gradient microscopy using a system of multifunctional metasurfaces," Nat. Photonics **14**(2), 109–114 (2020).
22. Z. Wang, L. J. Millet, M. U. Gillette, and G. Popescu, "Jones phase microscopy of transparent and anisotropic samples," Opt. Lett. **33**(11), 1270–1272 (2008).
23. P. Kocsis, I. Shevkunov, V. Katkovnik, and K. Egiazarian, "Single exposure lensless subpixel phase imaging: optical system design, modelling, and experimental study," Opt. Express **28**(4), 4625–4637 (2020).
24. G. Zheng, R. Horstmeyer, and C. Yang, "Wide-field, high-resolution Fourier ptychographic microscopy," Nat. Photonics **7**(9), 739–745 (2013).
25. Y. Cotte, F. M. Toy, C. Arfire, S. S. Kou, D. Boss, I. Bergoënd, and C. Depeursinge, "Realistic 3d coherent transfer function inverse filtering of complex fields," Biomed. Opt. Express **2**(8), 2216–2230 (2011).
26. C. J. Sheppard, S. S. Kou, and J. Lin, "The Green-function transform and wave propagation," Front. Phys. **2**, 67 (2014).
27. H. F. Arnoldus, "Representation of the near-field, middle-field, and far-field electromagnetic green's functions in reciprocal space," J. Opt. Soc. Am. B **18**(4), 547–555 (2001).
28. C. Sheppard, "Focal distributions and Hertz potentials," Opt. Commun. **160**(4-6), 191–194 (1999).
29. L. Novotny and B. Hecht, *Principles of Nano-Optics* (Cambridge University, 2012).
30. L. Hu, R. Chen, K. Agarwal, C. J. Sheppard, J. C. Phang, and X. Chen, "Dyadic green's function for aplanatic solid immersion lens based sub-surface microscopy," Opt. Express **19**(20), 19280–19295 (2011).
31. K. Agarwal, R. Chen, L. S. Koh, C. J. Sheppard, and X. Chen, "Crossing the resolution limit in near-infrared imaging of silicon chips: targeting 10-nm node technology," Phys. Rev. X **5**(2), 021014 (2015).
32. R. Chen, K. Agarwal, C. J. Sheppard, and X. Chen, "Imaging using cylindrical vector beams in a high-numerical-aperture microscopy system," Opt. Lett. **38**(16), 3111–3114 (2013).
33. S. F. Gibson and F. Lanni, "Experimental test of an analytical model of aberration in an oil-immersion objective lens used in three-dimensional light microscopy," J. Opt. Soc. Am. A **8**(10), 1601–1613 (1991).
34. X. Yang, H. Xie, E. Alonas, Y. Liu, X. Chen, P. J. Santangelo, Q. Ren, P. Xi, and D. Jin, "Mirror-enhanced super-resolution microscopy," Light: Sci. Appl. **5**(6), e16134 (2016).
35. A. K. Swan, L. A. Moiseev, C. Cantor, B. Davis, S. Ippolito, W. C. Karl, B. B. Goldberg, and M. Unlu, "Toward nanometer-scale resolution in fluorescence microscopy using spectral self-interference," IEEE J. Select. Topics Quantum Electron. **9**(2), 294–300 (2003).
36. K. Elsayad, A. Urich, P. S. Tan, M. Nemethova, J. V. Small, K. Unterrainer, and K. G. Heinze, "Spectrally coded optical nanosectioning (specon) with biocompatible metal–dielectric-coated substrates," Proc. Natl. Acad. Sci. **110**(50), 20069–20074 (2013).
37. H. S. Heil, B. Schreiber, R. Götz, M. Emmerling, M.-C. Dabauvalle, G. Krohne, S. Höfling, M. Kamp, M. Sauer, and K. G. Heinze, "Sharpening emitter localization in front of a tuned mirror," Light: Sci. Appl. **7**(1), 99 (2018).
38. A. Archetti, E. Glushkov, C. Sieben, A. Stroganov, A. Radenovic, and S. Manley, "Waveguide-paint offers an open platform for large field-of-view super-resolution imaging," Nat. Commun. **10**(1), 1267 (2019).
39. W. C. Chew, *Waves and Fields in Inhomogeneous Media* (Wiley-IEEE, 1995).
40. H. Guo, S. Zhuang, J. Chen, and Z. Liang, "Multilayered optical memory with bits stored as refractive index change. I. Electromagnetic theory," J. Opt. Soc. Am. A **24**(6), 1776–1785 (2007).
41. S. Wiersma, P. Török, T. Visser, and P. Varga, "Comparison of different theories for focusing through a plane interface," J. Opt. Soc. Am. A **14**(7), 1482–1490 (1997).
42. O. Haeberlé, "Focusing of light through a stratified medium: a practical approach for computing microscope point spread functions. Part I: Conventional microscopy," Opt. Commun. **216**(1-3), 55–63 (2003).
43. P. Török, P. Varga, Z. Laczik, and G. Booker, "Electromagnetic diffraction of light focused through a planar interface between materials of mismatched refractive indices: an integral representation," J. Opt. Soc. Am. A **12**(2), 325–332 (1995).
44. J. A. Kong, "Green's functions for planarly layered media," Tech. rep., Massachusetts Institute of Technology (2003).
45. R. Chen, K. Agarwal, Y. Zhong, C. J. Sheppard, J. C. Phang, and X. Chen, "Complete modeling of subsurface microscopy system based on aplanatic solid immersion lens," J. Opt. Soc. Am. A **29**(11), 2350–2359 (2012).
46. R. Chen, K. Agarwal, C. J. Sheppard, J. C. Phang, and X. Chen, "Resolution of aplanatic solid immersion lens based microscopy," J. Opt. Soc. Am. A **29**(6), 1059–1070 (2012).
47. C. J. Sheppard, T. J. Connolly, J. Lee, and C. J. Cogswell, "Confocal imaging of a stratified medium," Appl. Opt. **33**(4), 631–640 (1994).
48. W. L. Stutzman and G. A. Thiele, *Antenna Theory and Design* (John Wiley & Sons, 2012).